



## High-valent iron-oxo species mediated cyclic oxidation through single-atom $\equiv\text{Fe-N}_6$ sites with high peroxyomonosulfate utilization rate

Zhiwei Wang <sup>a</sup>, Wenlong Wang <sup>a</sup>, Jin Wang <sup>c</sup>, Yi Yuan <sup>a</sup>, Qianyuan Wu <sup>a,\*</sup>, Hongying Hu <sup>a,b,\*\*</sup>

<sup>a</sup> Key Laboratory of Microorganism Application and Risk Control of Shenzhen, Guangdong Provincial Engineering Research Center for Urban Water Recycling and Environmental Safety, Institute of Environment and Ecology, Tsinghua-Berkeley Shenzhen Institute, Tsinghua Shenzhen International Graduate School, Tsinghua University, Shenzhen 518055, PR China

<sup>b</sup> Environmental Simulation and Pollution Control State Key Joint Laboratory, Beijing Laboratory for Environmental Frontier Technologies, School of Environment, Tsinghua University, Beijing 100084, PR China

<sup>c</sup> College of Materials Science and Engineering, Shenzhen University, Shenzhen 518071, PR China



### ARTICLE INFO

#### Keywords:

Single Fe atom  
Peroxyomonosulfate activation  
High-valent iron-oxo species  
Oxidant utilization rate

### ABSTRACT

Fe singly anchored onto graphite carbon nitride (Fe-SA/PHCNS) as  $\equiv\text{Fe-N}_6$  was synthesized to realize efficient peroxyomonosulfate (PMS) activation and superior organic pollutant oxidation. The  $\equiv\text{Fe-N}_6$  was the core catalytic site of activation via forming high-valent iron-oxo species ( $\equiv\text{FeN}_6=\text{O}$ ) as the transient reactive intermediate as evidenced by X-ray adsorption fine spectroscopy (XAFS), in-situ Raman spectrum and theoretical calculation. The cycle of  $\equiv\text{Fe-N}_6$  and  $\equiv\text{FeN}_6=\text{O}$  interconversion was sustainably observed with organic pollutant as the electron-donor and PMS as the electron-acceptor. As results, the equivalent steady state concentration of  $\equiv\text{FeN}_6=\text{O}$  was as high as  $2.39 \times 10^{-8}$  M and this system exhibited 97.2% average PMS utilization rate. Fe-SA/PHCNS can be immobilized onto carbon felt for the simultaneous filtration and oxidation with stable and efficient performance. This study elucidated the mechanism and superiority of  $\equiv\text{FeN}_6=\text{O}$  mediated oxidation pathway and can advance the research and application of this new approach in advanced oxidation processes.

### 1. Introduction

Heterogeneous catalysis is attracting increasing interest for eliminating recalcitrant organic pollutants during wastewater purification and water reuse because of its advantages over homogeneous catalysis, such as better recoverability, lower chemical consumption, and negligible sludge waste production. However, heterogeneous catalysis has not been widely used in water purification because several challenges still need to be overcome, such as unsatisfactory intrinsic catalytic activity, insufficient exposure of active sites, limited oxidant utility, and potential metal leaching [1,2].

Single-atom catalysts (SACs) have recently been intensively investigated, and they are regarded as perfect candidates to solve the problems of conventional heterogeneous catalysts [3–8]. Compared with conventional catalysts, SACs can ultimately promote metal atom utilization through enhancing the accessibility of the metal atoms to the reactants [9], remarkably enhancing the intrinsic activity through low metal

coordination and effectively preventing metal leaching through strong metal-support interaction [10]. Moreover, SACs can be further optimized in terms of both their reactivity and selectivity through tuning the metal coordination environment [9]. Therefore, a perfect SACs used in catalytic oxidation for water purification should be optimized in terms of the electronic structure of the active-metal sites. In addition, the support is crucial for SAC preparation, activity promotion, and selectivity regulation. Graphitic carbon nitride ( $\text{g-C}_3\text{N}_4$ ) is an environmentally friendly material with high stability and low cost for advanced oxidation processes (AOPs) [11–14].  $\text{g-C}_3\text{N}_4$  contains abundant N atoms and it is a promising support for firmly trapping single metal atoms [15]. The metal–N–C active site is also a commonly used structure for reactive oxygen species (ROS) generation [16,17].

Fe is one of the most promising alternative active metals for catalytic oxidation, because it is not only naturally abundant and environmentally friendly, but it also shows relatively high activity for activating peroxides ( $\text{O}_2$ ,  $\text{H}_2\text{O}_2$  and persulfate) to form reactive species ( $\text{O}^*$  radical,

\* Correspondence to: Division of Energy and Environment, Tsinghua Shenzhen International Graduate School, Tsinghua University, Room 1810, Shenzhen 518055, PR China.

\*\* Correspondence to: School of Environment, Tsinghua University, Room 524, Beijing 100084, PR China.

E-mail addresses: [wuqianyuan@tsinghua.edu.cn](mailto:wuqianyuan@tsinghua.edu.cn) (Q. Wu), [hyhu@tsinghua.edu.cn](mailto:hyhu@tsinghua.edu.cn) (H. Hu).

$\cdot\text{O}_2$ ,  $\cdot\text{OH}$  and  $\text{SO}_4^{\cdot-}$ ). Numerous investigations and engineering practices have confirmed that Fe-based catalysis is an efficient and green method for organic pollutant removal in water or air [18,19]. For example, Zhang et al. have developed a  $\text{g-C}_3\text{N}_4$  supported Fe single-atoms catalyst ( $\text{Fe}_1/\text{CN}$ ) and achieved 100% selective production of  $\cdot\text{O}_2$  for highly selective and efficient degradation of pollutant [20]. Lei et al. have synthesized isolated  $\text{Fe}-\text{N}_x$  sites on  $\text{g-C}_3\text{N}_4$  to generate  $\text{O}^*$  radicals and exhibited efficient oxidative desulfurization with high sulfur selectivity [21]. Notably, a new oxidation mechanism via high-valent iron–oxo species, such as  $\text{Fe(IV)=O}$ ,  $\text{Fe(V)=O}$  and  $\equiv\text{FeN}_4=\text{O}$ , has recently been proposed for heterogeneous catalytic oxidation [22–26]. High-valent iron–oxo species are favorable for Fe-catalytic oxidation because they can overcome the conventional problems of AOPs. First, in comparison with the short lifetimes of radical species, high-valent iron–oxo species exist for several seconds (7–10 s) in water [27,28], which can enhance reactive species utilization. Second, high-valent iron–oxo species have strong oxidizing capacity and selectivity, which can focus the oxidizing capacity on the target organic pollutant. The above two points both endow high-valent iron–oxo species based oxidation system with high oxidant utilization rate which means that the consumed oxidants are mainly used for pollutant degradation rather than being wasted by radical self-decay or oxidizing background matrix. Third, in comparison with rate-limited conversion of  $\text{Fe(III)}$  to  $\text{Fe(II)}$ , the high-valent iron–oxo species mediated cyclic oxidation process can proceed rapidly in the presence of electron donors (e.g., organic pollutants), which sustainably drives catalytic oxidation of organic pollutants [22]. However, high-valent iron–oxo species with long lifetimes have not been realized in Fe SACs. In addition, the characteristics of high-valent iron–oxo species based oxidation, the transformation pathway of reactive Fe species and inner molecular mechanism of the high-valent iron–oxo species formation have not been well elucidated.

In this study, we used supramolecular aggregates pyrolysis method to fabricate porous hollow  $\text{g-C}_3\text{N}_4$  spheres with single Fe atoms (Fe-SA/PHCNS) and a novel  $\equiv\text{Fe-N}_6$  coordination configuration was constructed to activate peroxyomonosulfate (PMS). More nitrogen coordination regulated the electronic structure of singe Fe atom active sites and generated a special high-valent iron–oxo species ( $\equiv\text{FeN}_6=\text{O}$ ) with superior pollutant removal efficiency, good oxidation durability and high oxidant utilization rate (>90%). The  $\equiv\text{Fe-N}_6/\equiv\text{FeN}_6=\text{O}$  mediated cyclic oxidation process was illustrated through the combination of theoretical calculation and experiment. The  $\equiv\text{Fe-N}_6/\equiv\text{FeN}_6=\text{O}$  mediated cyclic oxidation process is spontaneous, sustainable, rapid, efficient, selective and stable. These results may motivate the research and application of high-valent iron–oxo species based oxidation system and guide rational design of single atom active sites for producing high-valent iron–oxo species.

## 2. Materials and methods

### 2.1. Chemicals

PMS ( $\text{KHSO}_5\text{-}0.5\text{KHSO}_4\text{-}0.5\text{ K}_2\text{SO}_4$ ), acetaminophen (ACE), melamine, cyanuric acid, iron nitrate hydrate ( $\text{Fe}(\text{NO}_3)_3\text{-}9\text{ H}_2\text{O}$ ), benzoic acid (BA), nitrobenzene (NB), and furfuryl alcohol (FFA) were purchased from Sigma Aldrich Co. Ltd., China. Dimethyl sulfoxide (DMSO), methyl phenyl sulfoxide (PMSO), potassium oxalate, sodium carbonate ( $\text{Na}_2\text{CO}_3$ ), sodium nitrate ( $\text{NaNO}_3$ ), sodium sulfate ( $\text{Na}_2\text{SO}_4$ ), sodium thiosulfate ( $\text{Na}_2\text{S}_2\text{O}_3$ ), and potassium thiocyanate (KSCN) were obtained from Macklin Co. Ltd., China. 5-*tert*-Butoxycarbonyl-5-methyl-1-pyrrolidine-*N*-oxide (BMPO, 99.0%) and 2,2,6,6-tetramethylpiperidinyloxy (TEMP) were purchased from DOJINDO Co. Ltd., China. All of the chemicals were analytical grade or better and directly used without further purification. Carbon felt sheet (thickness of  $5.4 \pm 0.2$  mm, void content of >90%, and BET surface area of  $0.22\text{ m}^2\text{ g}^{-1}$ ) was purchased from Beijing Jinglong Carbon Material Co., Ltd., China.

### 2.2. Preparation of Fe-SA/PHCNS

First,  $\text{Fe}(\text{NO}_3)_3\text{-}9\text{ H}_2\text{O}$  was dissolved in ultrapure water by ultrasonic treatment for 10 min and the final concentration of the Fe element was 20 g/l. Second, 1 g melamine was dissolved in 30 ml of DMSO and magnetically stirred for 30 min (solution A). The same operation was performed with 1 g of cyanuric acid (solution B). Next, 10 ml of iron nitrate solution was added to solution A and the solution was magnetically stirred for 30 min. Subsequently, solution B was slowly poured into solution A and a yellow precipitate formed. The mixture was then magnetically stirred for another 30 min. Yellow powder precursors were obtained by filtration and washed with 500 ml of ultrapure water. The precursor was dried in vacuum at 60 °C for 8 h and then completely ground. Finally, the powdered precursors were heated to 550 °C in a tube furnace with a ramp rate of 2.3 °C/min and kept for 4 h in a  $\text{N}_2$  atmosphere. The resultant products were ground and washed with ultrapure water several times to remove the impurities. PHCNS was synthesized by the same procedure without introducing iron nitrate.

### 2.3. Preparation of 3D-Fe-SA/PHCNS Sponge (FSPS)

The pristine carbon felt was cut into circles with 25 mm diameter, 5 mm thick. Next, 0.1 g of Fe-SA/PHCNS and 0.025 g of polyvinylidene fluoride (PVDF) were mixed with 5 ml of *N*-methyl pyrrolidone (NMP) solution and stirred for 4 h. Carbon felt was then immersed in the solution for 10 min and dried in vacuum at 80 °C for 8 h. The fresh FSPS was washed with ultrapure water several times.

### 2.4. Analytical Methods

The morphology and size of the catalyst were determined by scanning electron microscopy (SEM, GeminiSEM 300, ZEISS, 5 kV acceleration voltage) and transmission electron microscopy (TEM, JEM-3200FS, JEOL, 300 kV acceleration voltage). The high angle annular dark field scanning transmission electron microscopy (HAADF-STEM) images were recorded in STEM mode with an FEI Titan Themis Z scanning transmission electron microscope with double aberration correctors. The Brunauer–Emmett–Teller surface area and Barrett–Joyner–Halenda (BJH) pore volume were measured by an ASAP 2020 M+C analyzer. The X-ray diffraction pattern (XRD) was recorded with a Rigaku D/Max-rC powder diffractometer with  $\text{Cu K}\alpha$  radiation (1.5418 Å). X-ray photoelectron spectroscopy (XPS, Thermo Fisher ESCALAB 250Xi) was performed to analyze the surface composition and valence states of the different elements in the catalyst. Fe loading in the solid catalyst and Fe ion leaching were detected by an Optima 7300 DV inductively coupled plasma mass spectrometer (ICP-MS). The electron paramagnetic resonance (EPR) spectra was recorded a Bruker EMX plus spectrometer at room temperature. In-situ Raman spectra were recorded on a Renishaw confocal micro-Raman spectroscopy system with a 405 nm excitation laser.

### 2.5. XAFS Measurements

The X-ray absorption fine structure (XAFS) spectra of the Fe K ( $E_0 = 7112.0$  eV) edge was recorded at beamline 7-3 of the Stanford Synchrotron Radiation Laboratory (SSRL). The XAFS data were recorded in fluorescence mode with a Si (220) monochromator. The data were collected under ambient conditions and the absorption edge of pure Cu foil was used to calibrate the energy.

The obtained XAFS data were processed by Athena (version 0.9.26) for background, pre-edge line, and post-edge line calibration. Fourier transform fitting was then performed by Artemis (version 0.9.26). The  $k^3$  weighting,  $k$  range of  $2.2\text{--}8.2\text{ \AA}^{-1}$  and  $R$  range of  $1.0\text{--}2.2\text{ \AA}$ , was used for fitting the Fe sample, and the  $k$  range of 3 to  $\sim 12.6\text{ \AA}^{-1}$  and  $R$  range of  $1.0\text{--}3.0\text{ \AA}$  were used for fitting the Fe foil. The four parameters, coordination number, bond length, Debye–Waller factor, and  $E_0$  shift (CN, R,

$\sigma^2$ , and  $\Delta E_0$ ), were fitted without any of them fixed, constrained, or correlated. For wavelet transform analysis, the  $\chi(k)$  exported from Athena was imported into the Hama Fortran code. The parameters were as follows:  $R$  range of 1–4 Å,  $k$  range of 0–12.5 Å<sup>-1</sup>,  $k$  weight of 3, and Morlet function with  $\kappa = 5$ , and  $\sigma = 1$  was used as the mother wavelet to provide the overall distribution.

## 2.6. Experimental Procedures

To 60 ml of ACE (or another pollutant if necessary) solution, 6 mg of Fe-SA/PHCNS or PHCNS was added and the solution was magnetically stirred at 25 °C for 60 min to established adsorption–desorption equilibrium. A predetermined amount of sodium hydroxide was added to ensure that the initial pH was 7 after pouring into PMS. A certain amount

of PMS stock solution was added to the solution containing the pollutant and catalyst, and the reaction started. At specific time points, 0.5 ml sample was taken and mixed with 10 µL Na<sub>2</sub>S<sub>2</sub>O<sub>3</sub> (0.1 M) to rapidly quench the reaction. The mixture was then filtered by a cellulose acetate membrane (0.22 µm).

The concentration of the pollutant was measured by high-performance liquid chromatography (HPLC, SPD-M20A, Shimadzu) with a C18 reversed-phase column (Athena C18, 250 mm × 4.6 mm, CNW) and an UV detector. The dimethyl sulfone (DMSO<sub>2</sub>) was identified by gas chromatography–mass spectroscopy (GC-MS, Agilent, 7890B-5975 C). The degradation intermediates of ACE were identified by a high-resolution hybrid quadrupole Orbitrap mass spectrometer (Q Exactive, Thermo Fisher Scientific) equipped with an ultra-performance liquid chromatography (UPLC, Ultimate 3000, Thermo Fisher

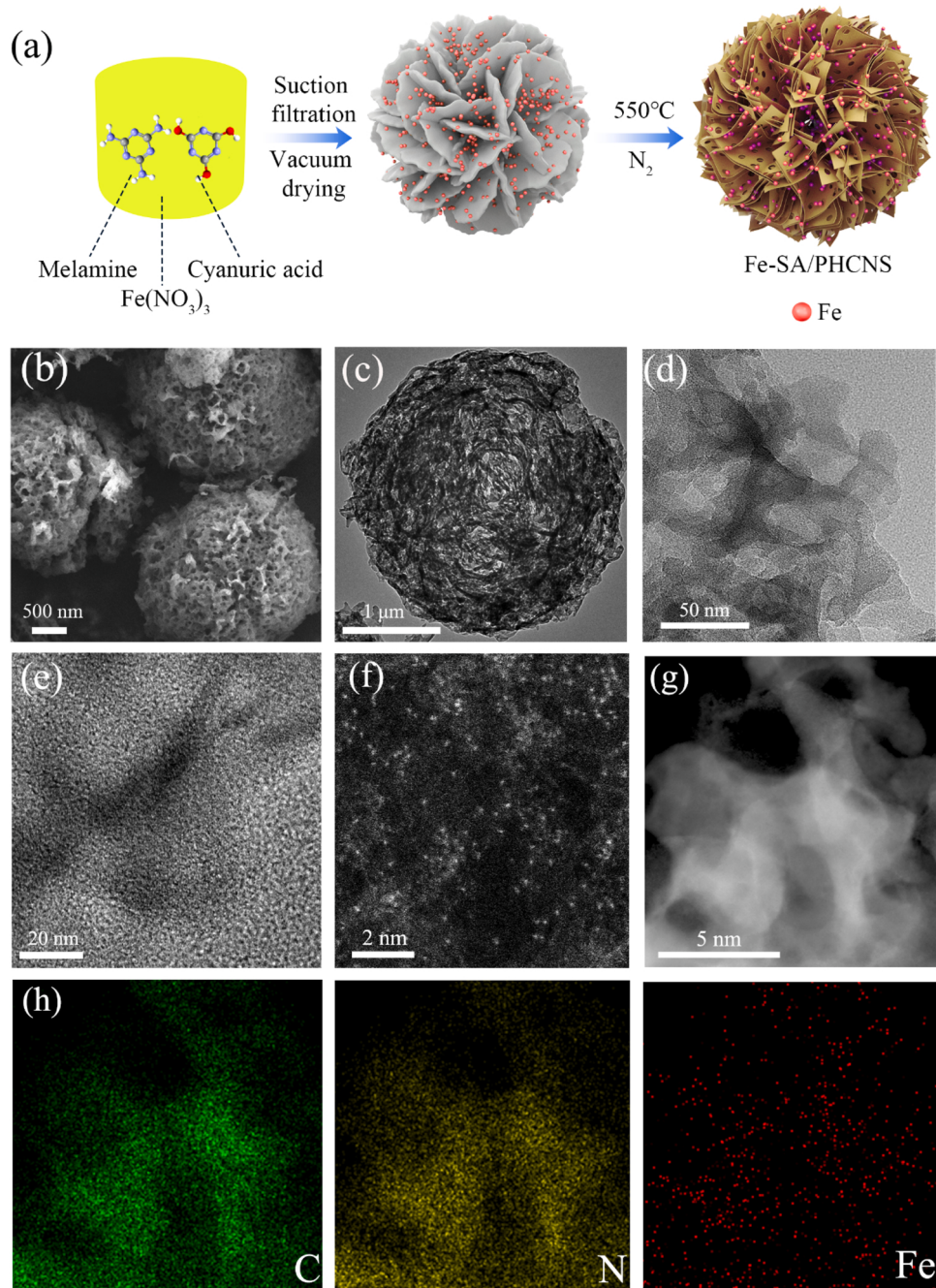


**Fig. 1.** (a) Illustration of synthesis of Fe-SA/PHCNS. (b) SEM. (c, d, e) HRTEM. (f) A high-resolution HAADF-STEM image. (g) HAADF-STEM image of Fe-SA/PHCNS and (h) Energy-dispersive X-ray elemental mapping of Fe-SA/PHCNS.

Scientific). A Hypersil Gold C18 column ( $2.1 \times 100$  mm,  $1.9\text{-}\mu\text{m}$  particle size, Thermo Fisher Scientific) was used for chromatographic separation. MS detection was operated in negative ion mode, with a mass-to-charge ratio ( $m/z$ ) scanning range of 50–500. Gradient of mobile phase increased from 5% methanol and 95% ultrapure water (v/v) to 95% methanol in 12 min. Then, it returned back to 5% methanol and kept for 3 min. Sample quantity is  $10\text{ }\mu\text{L}$  and the flow rate was  $0.3\text{ mL}/\text{min}$ . The concentrations of oxalate and thiocyanate were determined by ion chromatograph (ICS-900, Thermo Fisher Scientific).

## 2.7. Computational Models and Methodology

To elucidate the molecular mechanism of  $\equiv\text{FeN}_6 =\text{O}$  formation and the electronic structure, the single iron atom catalyst was simulated using a  $\text{C}_{27}\text{H}_{12}\text{N}_{36}\text{Fe}$  cluster model in which the Fe atom was bound to six pyridinic nitrogen atoms. Geometry optimization was performed with the Perdew–Burke–Ernzerhof hybrid functional (PBE0) [29] and def2-SVP basis set with Grimme’s DFT-D3(BJ) empirical dispersion correction [30] using the Gaussian 09 package [31]. The harmonic vibrational frequencies were computed at the same level of theory to obtain the Gibbs free energy. Using Multiwfn 3.7 [32] at the PBE0-D3 (BJ)/def2-TZVP level of theory, the RESP [33] (Restrained electrostatic potential) and Bader’s atomic charges were calculated to show the electron distribution, the quantum theory of atoms in molecules (QTAIM) [34] analysis were used to show the chemical bonds between atoms. The HOMO (highest occupied molecular orbital) and LUMO (lowest unoccupied molecular orbital) extracted from Multiwfn were viewed by VMD 1.9.3 [35]. Multiwfn was also used to derive the oxidation state of Fe in the molecules by the LOBA method [36] and Wiberg bond order [37] analysis was performed to determine the type of chemical bond.

## 3. Results and Discussion

### 3.1. Characterization of Fe-SA/PHCNS

Fe was atomically dispersed in and anchored to porous hollow  $\text{g-C}_3\text{N}_4$  spheres (Fe-SA/PHCNS) through thermal polymerization (Fig. 1a). Iron nitrate was first complexed with melamine to produce a melamine–Fe complex in dimethyl sulfoxide (DMSO) [38]. Cyanuric acid was then decanted, and hydrogen-bonded melamine–cyanuric acid (MCA) supramolecular aggregates complexed with Fe were formed to prevent aggregation of Fe during pyrolysis [39–41]. The supramolecular aggregates possessed structural similarity to  $\text{g-C}_3\text{N}_4$ , which can facilitate the condensation process and enable structural perfection [42,43]. The synthesized PHCNS contained C, N, and O, but not Fe, while Fe-SA/PHCNS contained Fe. The trace oxygen content (<5%) was attributed to absorbed  $\text{O}_2/\text{H}_2\text{O}$  (Fig. S1) [44].

Anchoring Fe to PHCNS slightly altered the external morphology of PHCNS, but it clearly increased the internal porosity of PHCNS. Scanning electron microscopy (SEM) and transmission electron microscopy (TEM) images (Fig. 1b, c, and S2) showed that both Fe-SA/PHCNS and PHCNS had regular porous hollow spherical structures with diameters of  $1\text{--}3\text{ }\mu\text{m}$ . However, Fe-SA/PHCNS was clearly more porous than PHCNS, as evidenced by the high-resolution TEM (HRTEM) images (Fig. S3). The  $\text{N}_2$  adsorption–desorption isotherms (Fig. S4) showed that the Brunauer–Emmett–Teller (BET) surface area increased from  $51.8$  to  $88.5\text{ m}^2/\text{g}$  and the Barrett–Joyner–Halenda (BJH) pore volume increased from  $0.28$  to  $0.80\text{ cm}^3/\text{g}$  by anchoring Fe to PHCNS. Additionally, two characteristic X-ray diffraction (XRD) peaks appeared at  $26.6^\circ$  and  $13.2^\circ$  (Fig. S5), which are assigned to (002) [45] interlayer stacking and (100) trigonal nitrogen linkage of  $\text{g-C}_3\text{N}_4$  [42]. Both of these peaks shifted to lower angle compared with  $\text{g-C}_3\text{N}_4$  synthesized by other methods, indicating an increased interlayer distance and looser structure. The lower intensity of the (002) facet for Fe-SA/PHCNS compared with bare PHCNS indicated that insertion of Fe atoms

distorted the crystal structure of  $\text{g-C}_3\text{N}_4$  by generating more pores. No peaks of iron/iron oxide particles were observed. Coordination of Fe to melamine will weaken the hydrogen bond between melamine and cyanuric acid and accelerate sublimation of melamine and cyanuric acid in thermal polymerization [42,46]. The porous hollow loose structure can increase the accessibility of single Fe atoms to reactants, subsequently endowing Fe-SA/PHCNS with enhanced catalytic performance [15].

Fe atomically dispersed on PHCNS without formation of nanoparticles or clusters, as evidenced by the HRTEM images and the bright spots in the high-angle annular dark-field scanning TEM (HAADF-STEM) images (Fig. 1d–f). The Fe atoms were uniformly dispersed on PHCNS (Fig. 1g and h). X-ray absorption fine structure (XAFS) measurements were performed to probe the electronic structure and coordination environment of Fe-SA/PHCNS. In the normalized Fe K-edge X-ray absorption near edge structure (XANES) spectrum (Fig. 2a), the rising edge of Fe-SA/PHCNS was located between those of  $\text{FeO}$  and  $\text{Fe}_3\text{O}_4$ , suggesting the oxidized  $\text{Fe}^{\delta+}$  ( $2 < \delta < 2.67$ ) state.

The Fe-anchored environment was analyzed by Fourier-transformed  $k^3$ -weighted extended X-ray absorption fine structure (EXAFS) spectroscopy and XPS. Coordination-unsaturated sites like N atoms in tri-s-triazine units are easily formed during thermal polymerization, which is crucial to atomically dispersion of Fe atom [47,48]. Atomic Fe dominantly bonded to the N atoms (average  $\text{Fe}-\text{N}$  peak at  $1.42\text{ \AA}$ ) in the tri-s-triazine units, as shown in Fig. 2b. No obvious Fe–Fe interaction was detected, indicating that the Fe atoms were atomically dispersed in the PHCNS matrix. In addition, Fe did not coordinate to C atoms, as evidenced by the similar C 1 s XPS spectra for PHCNS and Fe-SA/PHCNS (Fig. S6). Fe–N coordination was further corroborated by the  $5\text{ \AA}^{-1}$  peak in the EXAFS wavelet transform plots of Fe-SA/PHCNS and Iron phthalocyanine (FePc) (Fig. S7) [49]. The fitting curve with the first shell of  $\text{Fe}-\text{N}$  (Fig. 2c) indicated that the  $\text{Fe}-\text{N}$  bond distance in Fe-SA/PHCNS was about  $\sim 2.09\text{ \AA}$ , which is in the normal range [17]. The average coordination number of  $\text{Fe}-\text{N}$  in Fe-SA/PHCNS was  $\sim 5.9$  (Table S1). The N 1 s spectra showed that the dominant nitrogen species in both catalysts were the  $\text{sp}^2\text{ C}=\text{N}=\text{C}$  bonds in tri-s-triazine (pyridinic N), which are favorable for binding Fe atoms (Fig. 2d) [50,51]. Moreover, the XPS peak of Fe-SA/PHCNS attributed to pyridinic N shifted to higher binding energy compared with PHCNS alone, indicating that the chemical state of the N atom in the tri-s-triazine unit changed after Fe modification. Specifically, the lone-pair electrons of the N atom in the tri-s-triazine unit occupied the free orbital of the central Fe atom to form  $\text{Fe}-\text{N}_x$  moieties, leading to a decrease in the outer shell electron density of the nitrogen atom and an increase in the binding energy [44,52]. All of these results verified the Fe–N interaction in Fe-SA/PHCNS. Moreover,  $\equiv\text{Fe-N}_6$  coordination configuration was rarely reported. The coordination number will hugely affect the intrinsic catalytic activity and catalytic mechanism, even with the same metal and support. Further exploration of the degradation performance and catalytic oxidation mechanism of  $\equiv\text{Fe-N}_6$  coordination configuration is meaningful to motivate the research about the effect of coordination number on single atom catalyst based heterogeneous catalytic oxidation.

### 3.2. Degradation Performance of Fe-SA/PHCNS/PMS System

FePc was highly active for PMS activation [53], which resulted in rapid ACE degradation by FePc/PMS (Fig. S8). The observed rate constant ( $k_{\text{obs}}$ ) was modified by the masses of PMS and the catalyst ( $k_{\text{spe}} = k_{\text{obs}}/(m_{\text{PMS}} \times m_{\text{cat}})$ , Text S1) to comprehensively show the capacity of PMS usage by Fe-SA/PHCNS per mass. The  $k_{\text{spe}}$  for FePc/PMS system is about  $10\text{ s}^{-1}\text{ g}^{-2}$ , which is much higher than conventional catalysts (Table S2). It is worth noting that Fe-SA/PHCNS showed analogue Fe–N coordination to FePc (Fig. S7). Therefore, Fe-SA/PHCNS has the potential to show excellent PMS activation performance.

Fe-SA/PHCNS could actually activate PMS and then enhanced ACE degradation from 17% within 30 min for PHCNS/PMS to > 99% within 8 min for Fe-SA/PHCNS (Fig. 3a). The ACE degradation by Fe-SA/

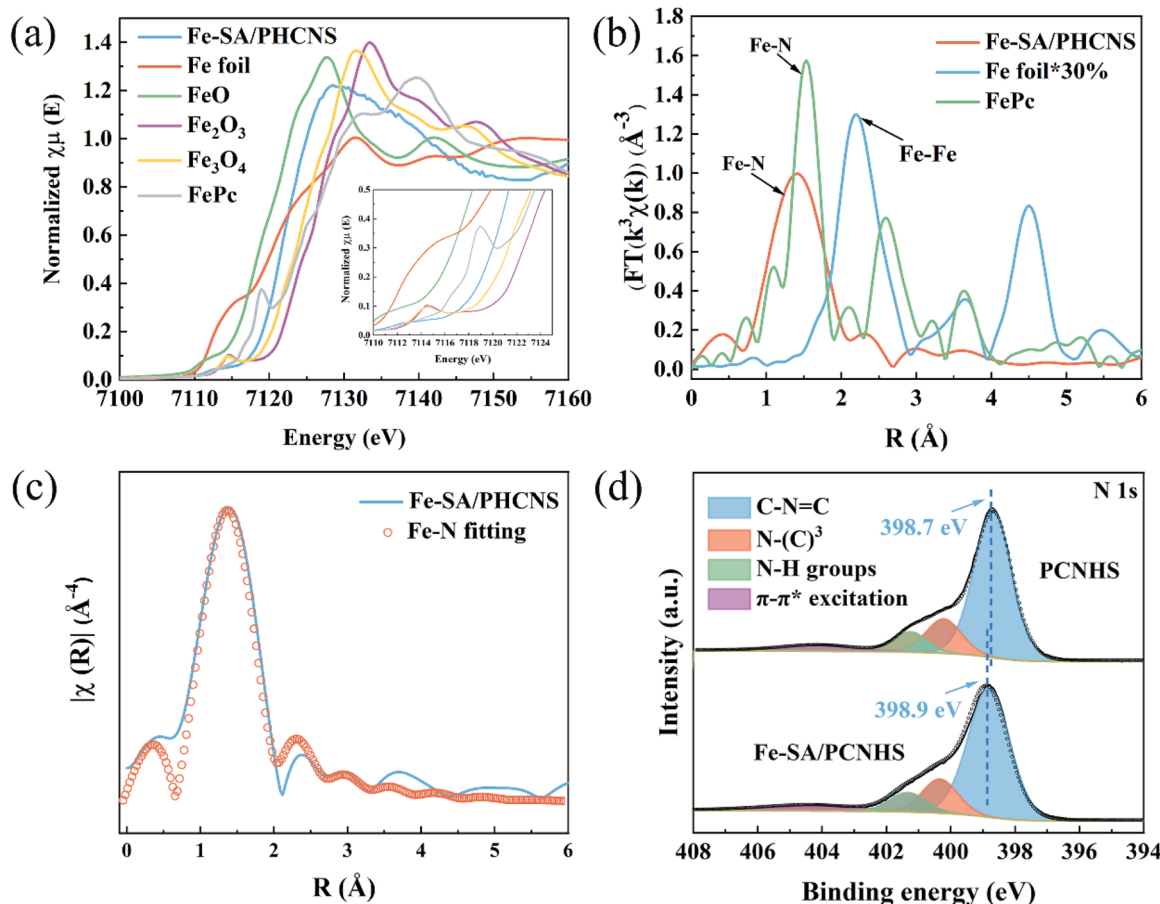


**Fig. 2.** (a) Normalized Fe K-edge XANES spectra of Fe foil, FeO, Fe<sub>2</sub>O<sub>3</sub>, Fe<sub>3</sub>O<sub>4</sub>, FePc, and Fe-SA/PHCNS. (b)  $k^3$ -weighted Fourier transform spectra from Fe K edge EXAFS and (c) the corresponding EXAFS fitting curve of Fe-SA/PHCNS. (d) N 1 s XPS spectra of Fe-SA/PHCNS and bare PHCNS.

PHCNS/PMS system followed pseudo-first-order kinetics (Fig. S9). For Fe-SA/PHCNS/PMS,  $k_{\text{spe}} = 0.364 \text{ s}^{-1} \text{ g}^{-2}$ , which was clearly better than other heterogeneous PMS activators for ACE degradation and performed higher PMS activation efficiency comparing to other phthalocyanine supported catalysts (Table S2). The C-C or C-N bonds in g-C<sub>3</sub>N<sub>4</sub> alone hardly activate PMS as evidenced by the negligible PMS decay and ACE degradation (Fig. 3a, S20). However, g-C<sub>3</sub>N<sub>4</sub> as support is crucial for catalyst preparation and degradation process. The nitrogen atoms in tri-s-triazine unit are helpful to stabilize single Fe atoms during calcination. Meanwhile, the six lone-pair electrons in the nitrogen pots could lead to the chemical bonding between Fe and N. Therefore, the electronic structure was regulated and the dissolution of metal ions was reduced. The mesoporous hollow spherical morphology of g-C<sub>3</sub>N<sub>4</sub> is also beneficial to promote accessibility of single Fe atoms to reactants. PMS oxidation activated by homogeneous Fe<sup>2+</sup> and Fe<sup>3+</sup> ions showed insignificant ACE degradation (Fig. S10).

### 3.3. Reactive species identification of Fe-SA/PHCNS/PMS System

Although the Fe-atom sites of Fe-SA/PHCNS can active PMS to form ROS (e.g., •OH, SO<sub>4</sub><sup>•-</sup>, and <sup>1</sup>O<sub>2</sub>), the ROS contributions were insignificant. Formation of ROS was verified by the electron paramagnetic resonance (EPR) spectra of the 5-tert-Butoxycarbonyl-5-methyl-1-pyrroline-N-oxide (BMPO)-•OH, BMPO-SO<sub>4</sub><sup>•-</sup>, and 2,2,6,6-tetramethylpiperidinyloxy (TEMP)-<sup>1</sup>O<sub>2</sub> adducts (Fig. 3b and c) [54]. According to the electronegativity difference, the electrons of Fe atoms were grabbed by surrounding N/C atom and formed electron-deficient Fe atoms for the generation of <sup>1</sup>O<sub>2</sub> by oxidizing PMS. At the same time, the electron rich N/C atom could act as electron-rich center for the formation of •OH and

SO<sub>4</sub><sup>•-</sup> by PMS reduction [55]. However, ethanol (EtOH, quencher for •OH and SO<sub>4</sub><sup>•-</sup>) and tert-butyl alcohol (TBA, quencher for •OH) only slightly suppressed ACE degradation [56]. Furfuryl alcohol (FFA, quencher for <sup>1</sup>O<sub>2</sub> and •OH) showed significant inhibition (Fig. 3d). The ROS contributions were quantified with ROS probes and competing kinetics calculation (Fig. S11, Text S2). The contributions of •OH and SO<sub>4</sub><sup>•-</sup> accounted for only 4.7% and 14.8% of the total ACE degradation by Fe-SA/PHCNS/PMS, respectively (Fig. 3e). Because FFA does not only react with <sup>1</sup>O<sub>2</sub>, the contribution of <sup>1</sup>O<sub>2</sub> should be overestimated. However, the second-order rate constant of <sup>1</sup>O<sub>2</sub> with molecular ACE (APOH) is only  $3.35 \times 10^5 \text{ M}^{-1} \text{ s}^{-1}$  owing to the low electron density on the aromatic ring [57,58]. Almost all of ACE is present as APOH at pH < 7 (Fig. S12), and thus even the overestimated contribution of <sup>1</sup>O<sub>2</sub> is negligible (Fig. 3e).

The superior activation performance was caused by the Fe-atom sites, because the oxidation performance was dramatically suppressed when oxalate and thiocyanate were used to chelate the Fe atoms. The occupation by chelates would block the accessibility of active sites and resulted in lowering  $k_{\text{spe}}$  to 0 and  $0.04 \text{ s}^{-1} \text{ g}^{-2}$ , respectively (Fig. 3f). Meanwhile, oxalate and thiocyanate were hardly degraded (Fig. S13), indicating that the inhibition effect did not result from their direct competition with ACE for the reactive species.

Besides ROS, Fe-SA/PHCNS can active PMS to form other reactive species, such as high-valent iron–oxo species (e.g.,  $\equiv\text{Fe}(\text{IV})=\text{O}$  and  $\equiv\text{Fe}(\text{V})=\text{O}$ ) [22,23,59]. To verify this, in-situ Raman with a 405 nm excitation laser and XANES were used to investigate the surface chemical evolution of  $\equiv\text{Fe}-\text{N}_6$  sites during activating PMS. In comparison to Fe-SA/PHCNS alone and PMS alone, Fe-SA/PHCNS/PMS showed a new peak at  $880 \text{ cm}^{-1}$  in the Raman spectra (Fig. S14), which may be

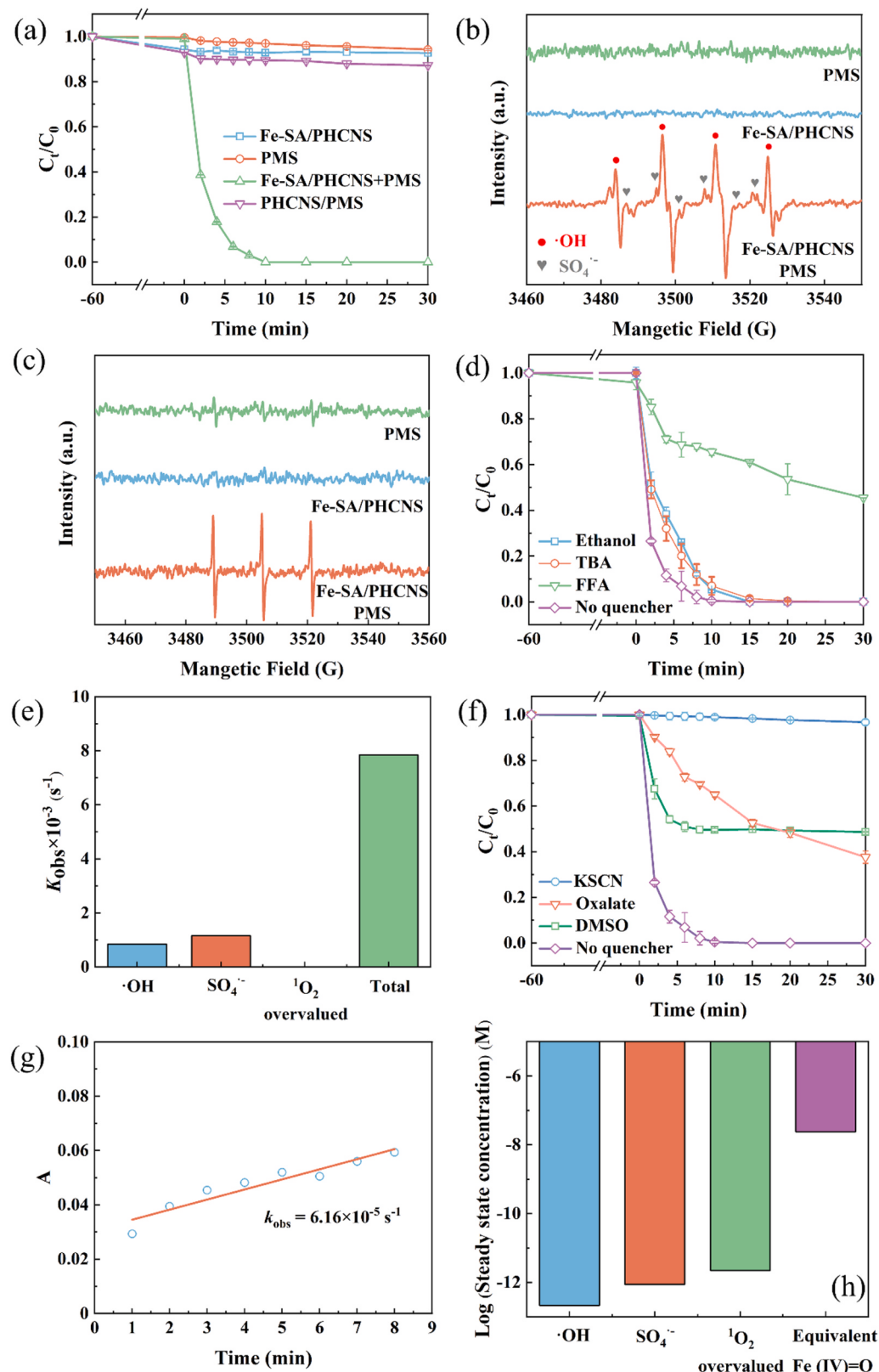


**Fig. 3.** (a) Degradation of ACE by activating PMS in different reaction systems. (b, c) EPR spectra of the different systems captured by BMPO (25 mM) and TEMP (60 mM). (d) Quenching experiments of the Fe-SA/PHCNS/PMS system using EtOH (0.5 M), TBA (0.5 M), and FFA (0.01 M) as scavengers. (e) Contributions of different active species to ACE degradation in the Fe-SA/PHCNS/PMS system. (f) Influence of KSCN (5 mM), oxalate (25 mM), and DMSO (0.1 M) on ACE degradation. (g) Pseudo-first-order kinetic model fitting of  $\text{PMSO}_2$  generation ( $A$  denotes  $\ln \frac{[\text{PMSO}_2]}{[\text{PMSO}]_0} - \frac{1}{2} \ln [\text{PMSO}_2]$ ). (h) Steady-state concentration of ROS. Reaction condition: [Catalyst] = 0.1 g/L, [PMS] = 0.2 g/L, [ACE] = 10 mg/L, initial pH = 7, T = 298 K.

ascribed to the vibration of Fe=O in high-valent iron-oxo species [60, 61]. Comparing to the six-coordinate oxo-ferryl porphyrins ( $760\text{--}840\text{ cm}^{-1}$ ), there was a blue shift for the Fe=O vibration frequencies which may indicate the strong interaction between Fe and O atom. The peak intensity kept relatively constant over time may exhibited the long lifetime of high-valent iron-oxo species. For XANES spectra, the higher valence state of Fe, the K-edge position tends to shift toward higher energy [62]. As shown in Fig. S15, Fe K-edge position has a significant shift to the higher energy region after adding PMS. The energy edge (the maximum position of the first derivative near the absorption edge) increased from 7120.5 eV to 7124.1 eV which was

ascribed to the formation of high-valent iron-oxo species. White line peak intensity is another important index for valence state analysis which is correlated with the occupation of the outermost orbital. Higher valence state means outermost orbital occupation decrease. More inner electrons could be excited to the outermost electron orbits which cause a stronger absorption of X-rays and higher white line peak intensity [63]. The intensity of white line peak increased after PMS oxidation indicated a more oxidized Fe valence state. Moreover, the specific O-atom-transfer reaction from sulfoxides to sulfones was employed to further verify the generation of high-valent iron-oxo species. DMSO was used to react with the high-valent iron-oxo species. DMSO inhibited 76.2% of ACE

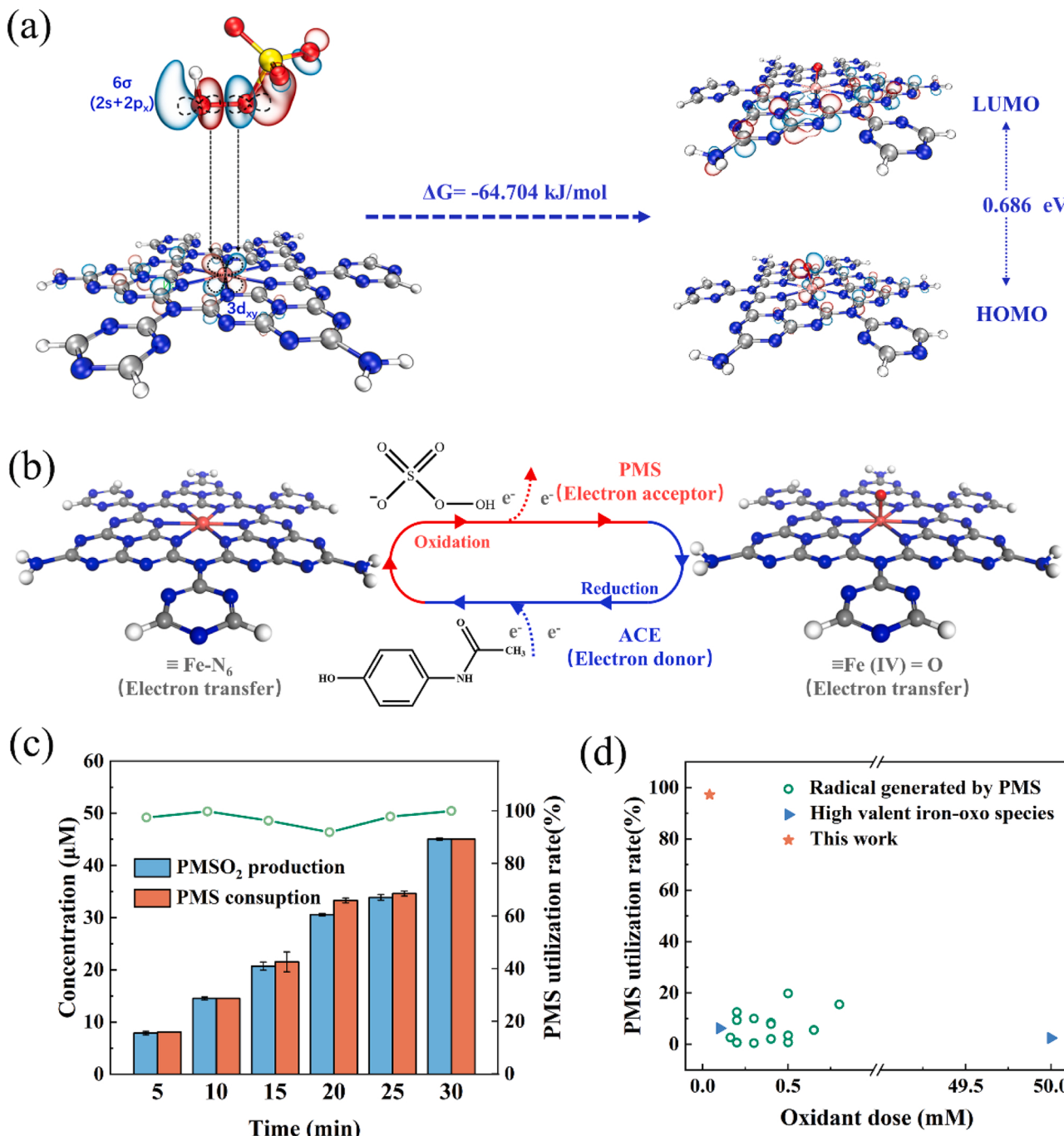


**Fig. 4.** (a) Symmetry matching between the LUMO of  $\text{HSO}_5^-$  and HOMO of Fe-SA/PHCNS. The blue and red shadows represent the frontier molecular orbitals. (b) Illustration of  $\equiv\text{Fe}(\text{IV})=\text{O}$  mediated cyclic reaction mechanism. (c) PMS utilization rate in the Fe-SA/PHCNS system. Reaction condition: [Catalyst] = 0.1 g/L, [PMSO<sub>2</sub>] = 1 mM, [PMS] = 0.25 mM, [ACE] = 10 mg/L, initial pH = 7, T = 298 K. (d) Comparison of PMS utilization rate between the Fe-SA/PHCNS system and other catalysts.

degradation and formed dimethyl sulfone ( $\text{DMSO}_2$ ) through the specific O-atom-transfer reaction from sulfoxides to sulfones (Fig. 3f and S16) [64]. Quinones of 1,4-benzoquinone, hydroquinone, and some dimers, which are formed by phenolic compound oxidation, were identified by liquid chromatography coupled with mass spectroscopy (LC-MS), which is consistent with the oxidation pathway by high-valent iron species (Fig. S17) [65,66].  $\text{DMOS}_2$  production, together with the XANES result verifies that a high-valent iron was formed in Fe-SA/PHCNS. To quantify the importance of the high-valent iron-oxo species during Fe-SA/PHCNS/PMS activation, a high-valent iron-oxo species equivalent was assessed through degradation of methyl phenyl sulfoxide (PMSO) and the corresponding formation of  $\text{PMSO}_2$  (Fig. 3g and S18, and Text S3). The equivalent steady state concentration of  $\equiv\text{FeN}_6=\text{O}$  was as high as  $2.39 \times 10^{-8} \text{ M}$ , which was almost five orders of magnitude higher than other ROS (Fig. 3h). It has been reported that high-valent iron-oxo species show strong degradation activity towards ACE in other systems [59,67–69]. Therefore, high-valent iron-oxo species generated by Fe-SA/PHCNS/PMS should be responsible for the ACE degradation.

### 3.4. Characteristics and Mechanism of Cyclic $\equiv\text{Fe-N}_6/\equiv\text{FeN}_6=\text{O}$ Oxidation

Cyclic  $\equiv\text{Fe-N}_6/\equiv\text{FeN}_6=\text{O}$  oxidation is a spontaneous, rapid, sustainable, efficient, selective and stable process. Theoretical calculations were performed to investigate spontaneous formation of  $\equiv\text{FeN}_6=\text{O}$  during Fe-SA/PHCNS/PMS activation.

#### 3.4.1. Spontaneous

PMS can spontaneously adsorb to Fe-SA/PHCNS owing to the low adsorption energy ( $E_{\text{ads}} = -184.8 \text{ kJ/mol}$ ). The lowest unoccupied molecular orbital (LUMO) of  $\text{HSO}_5^-$  (2 s and  $2p_x$  orbitals of the O atom connected to the H atom) possess orbital symmetry match (Fig. 4a) with the highest occupied molecular orbital (HOMO) of Fe-SA/PHCNS ( $\equiv\text{Fe-N}_6$ ), as shown in Fig. 4a. The charge transfer obeys the electronegativity variation tendency between the Fe atom and O atom, as evidenced by the Bader atomic charges and restrained electronic potential (RESP) (Table S3). According to frontier molecular orbital theory, the chemical absorption process preferentially occurs and chemical bonds form between Fe and O, which is verified by the bond critical point between these two atoms from the quantum theory of atoms in molecules (QTAIM) analysis (Fig. S19).

Moreover, the transient intermediate state ( $\text{N}_6-\text{Fe-PMS}$ ) is unstable because the HOMO-LUMO gap is small (0.515 eV). There are two relatively unstable bonds in the transient intermediates: Fe-O and O-O bonds. Because the Fe-O bond has higher Wiberg bond order (1.38) and bond energy (561 kJ/mol) than the O-O bond (0.70 and 377 kJ/mol, respectively) (Tables S4 and S5), O-O cleavage preferentially occurs over Fe-O cleavage. This process is thermodynamically spontaneous because the Gibbs free energy ( $\Delta G$ ) is negative ( $-64.78 \text{ kJ/mol}$ ) (Table S6). The increase in the atomic charges suggests a more positive valence state of Fe in Fe-O, which increases from II to IV based on localized orbital bonding analysis (LOBA) theory (Tables S3 and S7). Therefore, the Fe-SA/PHCNS/PMS system would preferentially and dominantly form  $\equiv\text{FeN}_6=\text{O}$ . This process can proceed spontaneously because of the small  $\text{N}_6-\text{Fe-PMS}$  adsorption energy, relatively low O-O bond energy and negative  $\Delta G$ .

#### 3.4.2. Rapid and sustainable

Less than 15% PMS decomposed in the Fe-SA/PHCNS/PMS system without ACE, which indicates the slow self-decay of  $\equiv\text{FeN}_6=\text{O}$ . Because the slow self-decay of  $\equiv\text{FeN}_6=\text{O}$  could lead to the accumulation of reaction products which would block the reaction between PMS and  $\equiv\text{Fe-N}_6$  and result in slow PMS decomposition. It has been reported that the half-life of Fe(IV) is about 7 s at pH = 1 [27], and even longer at higher pH values [28]. The high-valent iron-oxo species with porphyrin

ligand was also reported to have a long lifetime [70]. Shan and Jr reported that the oxo ligand is crucial to the high charge mitigation of the Fe (IV)=O center. Neutral ligands are needed to stabilize the Fe (IV)=O unit [71].  $\text{g-C}_3\text{N}_4$  is an electrically neutral heterogeneous material with weak electrical conductivity. In the absence of electron donor, the high charge of Fe center is unable to release which endows  $\equiv\text{FeN}_6=\text{O}$  with long lifetime. However, in the presence of ACE, fast electron transfer occurs between  $\equiv\text{FeN}_6=\text{O}$  and ACE, which leads to rapid PMS decomposition (Fig. S20). PMS decomposition fitted the pseudo-first-order kinetic model well (Fig. S21, Text S4) which means that the number of  $\equiv\text{Fe-N}_6$  should be steady. There is a circular reaction between  $\equiv\text{Fe-N}_6$  and  $\equiv\text{FeN}_6=\text{O}$ .  $\equiv\text{Fe-N}_6$  transferred electrons to PMS and formed  $\equiv\text{FeN}_6=\text{O}$ , and then  $\equiv\text{FeN}_6=\text{O}$  was reduced back to  $\equiv\text{Fe-N}_6$  by the electron donor. In the absence of an electron donor,  $\equiv\text{FeN}_6=\text{O}$  cannot accept electrons, which leads to limited  $\equiv\text{Fe-N}_6$  regeneration and dramatic suppression of electron transfer to PMS and inhibits the PMS decomposition. Sustainable formation of  $\equiv\text{FeN}_6=\text{O}$  is schematically illustrated in Fig. 4b, in which the  $\equiv\text{Fe-N}_6/\equiv\text{FeN}_6=\text{O}$  circular reactions act as the electron-mediator of target pollutants reacting with PMS, including two steps: (1) electron acceptor (PMS) captured electron from mediator and form oxidizing intermediate ( $\equiv\text{FeN}_6=\text{O}$ ); (2) electron donor (ACE) supplies electron to reduce oxidizing intermediate back to original state ( $\equiv\text{Fe-N}_6$ ) and electron donor itself is oxidized (oxidative degradation).

#### 3.4.3. Efficient

$\equiv\text{Fe-N}_6/\equiv\text{FeN}_6=\text{O}$  circular reactions can utilize PMS efficiently, as evidenced by the electron-acceptor capacity of PMS being almost completely and rapidly dedicated to formation of  $\equiv\text{FeN}_6=\text{O}$ . The electron-transfer number was used to evaluate utilization of PMS. Reduction of PMS and oxidation of PMSO to generate  $\text{PMSO}_2$  are both two-electron-transfer pathways. Because production of  $\text{PMSO}_2$  is specific to  $\equiv\text{FeN}_6=\text{O}$  [23], the amount of  $\text{PMSO}_2$  generated can be used to represent production of  $\equiv\text{FeN}_6=\text{O}$ , and utilization of PMS can be further evaluated by the ratio of  $\text{PMSO}_2$  to PMS consumption (Text S5). With increasing reaction time,  $\text{PMSO}_2$  proportionally increased with the PMS consumption increase and the ratio remained higher than 91% (Fig. 4c). In comparison with previous studies, utilization of oxidant in this study was hundreds of times higher than other PMS activators or high-valent iron-oxo species generating systems (Fig. 4d and Table S8), which indicates the superior oxidant utilization performance of  $\equiv\text{Fe-N}_6/\equiv\text{FeN}_6=\text{O}$  circular reactions during Fe-SA/PHCNS/PMS activation.

#### 3.4.4. Selective

High oxidation selectivity can focus the oxidizing capacity on target pollutant degradation and also promote utilization of the oxidant. The Fe-SA/PHCNS/PMS system showed high reactivity for organic matter with electron-donating groups, such as thiazole, sulphydryl, hydroxyl, and amido groups [22,69,72], which are common in pollutants. However, for compounds with electron-withdrawing moieties, such as carboxyl groups, the degradation efficiencies were slightly lower (Fig. S22). The selectivity of Fe-SA/PHCNS/PMS represents the electrophilicity of  $\equiv\text{FeN}_6=\text{O}$  which accords closely with that of other high-valent iron-oxo species [22,73]. Multiple environmentally relevant anions ( $\text{Cl}^-$ ,  $\text{SO}_4^{2-}$ ,  $\text{NO}_3^-$ , and  $\text{CO}_3^{2-}$ ) had no influence on Fe-SA/PHCNS/PMS (Fig. S23), which is further evidence for the high selectivity of  $\equiv\text{FeN}_6=\text{O}$  [74,75]. Negligible halogenated byproducts were formed during the catalytic oxidation, which may be related to the relatively high selectivity of  $\equiv\text{FeN}_6=\text{O}$  can avoid the formation of hypochlorous or hypobromous acids [76,77]. Meanwhile, the structure uniformity of atomic dispersion of Fe further strengthened the selectivity. The Fe-SA/PHCNS system maintained excellent ACE degradation efficiency in a wide pH range (4–8) (Fig. S24). Low pH can enhance the reactivity of  $\equiv\text{FeN}_6=\text{O}$  [69,78,79], resulting in better degradation efficiency. However, for pH > 7, some of ACE was in anionic forms

(Fig. S12), and the surface of Fe-SA/PHCNS became more negatively charged and led to repulsion, which is unfavorable for ACE degradation.

### 3.4.5. Stable

Fe-SA/PHCNS showed outstanding stability, as evidenced by the high ACE elimination in recycling experiments. After five cycles of ACE degradation, the removal rate of ACE still could be 97.4% (Fig. S25). The stability of Fe-SA/PHCNS was further verified by the similar XPS spectra

of the fresh and used catalyst, which means good regenerability and resistance of  $\equiv\text{Fe}-\text{N}_6$  to ROS (Fig. S26).

Fe-SA/PHCNS was integrated on to a porous carbon fiber skeleton (FSPS) to verify its practical feasibility during water purification. The FSPS was prepared by a one-step immersion method (Fig. 5a). SEM images showed that Fe-SA/PHCNS was loaded on the carbon fiber skeleton (Fig. 5b). Thus, the catalytic performance can be maximized by increasing the number of available active sites in the three-dimensional

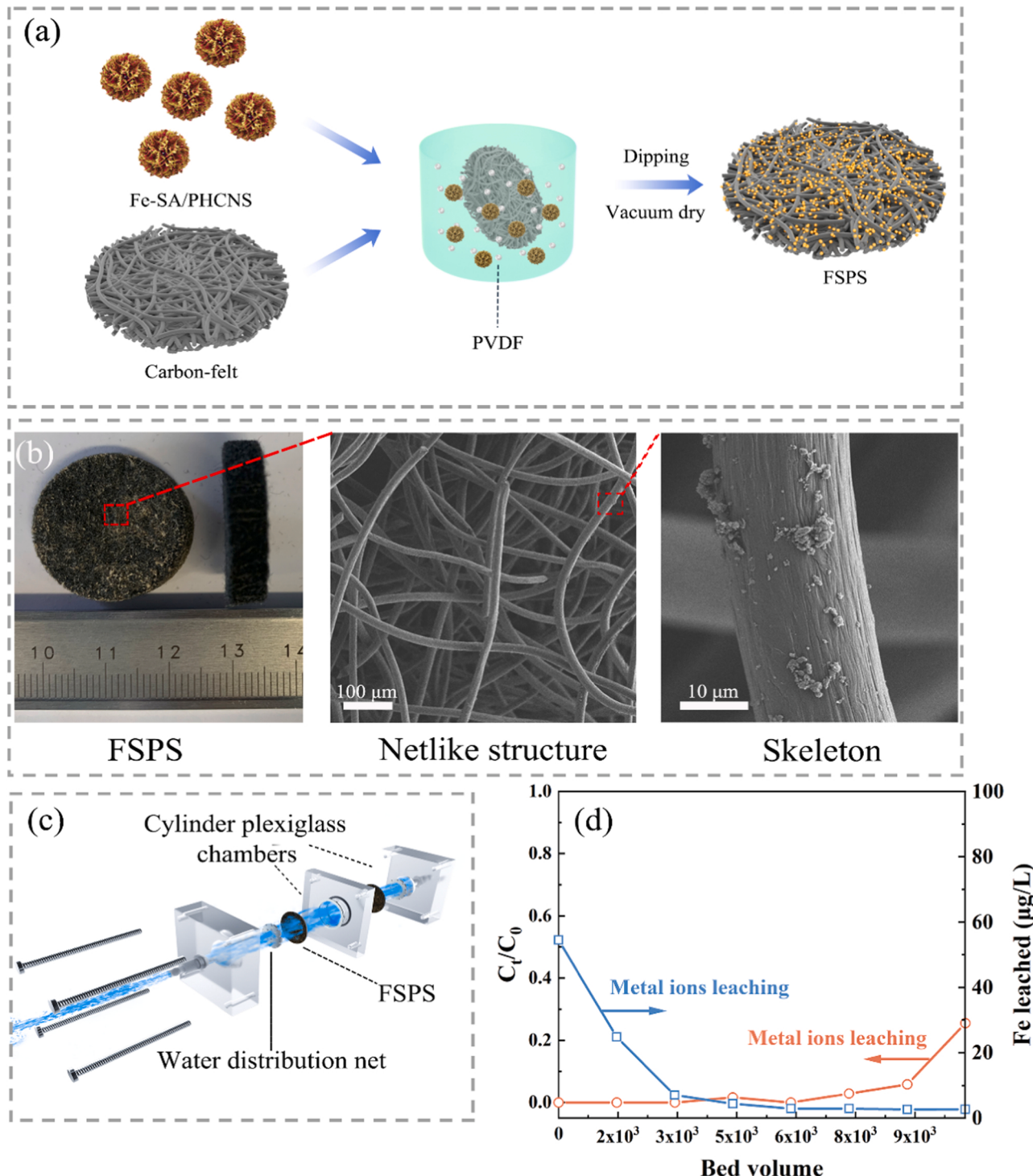


**Fig. 5.** (a) Illustration of the synthesis pathways of FSPS. (b) Images of FSPS. (c) Schematic illustration of flow-through reactor with FSPS filter. (d) Continuous operation test of ACE degradation and Fe leaching by the FSPS-based flow-through filter. Reaction condition: flow rate = 10 ml/min, Catalyst loading = 0.1 g, [PMS] = 0.2 g/L, [ACE] = 5 mg/L, initial pH = 7, T = 298 K. Bed volume (BV) is the volume of flow-through reactor which defines as the unit of treated water quantity.

(3D) netlike structures and enhancing pollutant mass transfer in turbulent flow.

The performance of FSPS was assessed by a flow-through reactor (Fig. 5c). Carbon felt was used as the support due to its high surface area and porosity. High surface area and porosity are beneficial for increasing catalyst loading and enhancing contact between reactive species and pollutants. Moreover, the porous structure of carbon felt can withstand water impact without affecting water penetration which is suitable to be used as high flow rate filter. The structural and chemical stability of carbon felt guarantee the long-term operation efficiency of filter [80]. A mixed solution of ACE and PMS was pumped through the FSPS filter with a flow rate of 10 ml/min, which was much higher than that of a generic filter [23,81]. The ratio of treated water to the bed volume was employed to assess the performance and stability of the synthesized 3D-Fe-SA/PHCNS Sponge filter. It was observed that the FSPS filter which only contained 0.1 g Fe-SA/PHCNS maintained 100% ACE removal efficiency for 24 h after 5867 BV and over 95% for 36 h after 10267 BV (Fig. 5d). Pure carbon felt with PMS and Fe-SA/PHCNS alone showed no degradation effect (Fig. S27). The strong metal–support interaction makes  $\equiv\text{Fe}-\text{N}_6=\text{O}$  resistant to scouring by water and oxidation by PMS. Negligible Fe leaching was observed during operation (Fig. 5d). The decrease of the removal efficiency to 75% after 10200 BV may be because of Fe-SA/PHCNS fall off from the carbon fiber.

#### 4. Conclusions

Although heterogenous AOPs has been implicated in water purification, the limited accessibility of active sites hinders the oxidant activation efficiency. Meanwhile, the ultra-short lifetimes and unselective oxidation both lead to low ROS utilization efficiency which result in the waste of oxidant. Thus, the low oxidant utilization rate of oxidant always impedes the further practical application of heterogenous AOPs. Here, we have synthesized the porous hollow  $\text{g-C}_3\text{N}_4$  spheres anchored with highly accessible single-Fe-atom active sites which is beneficial for oxidant activation. The  $\equiv\text{FeN}_6=\text{O}$  which is responsible for ACE degradation is relatively long-lasting and highly selective. Therefore,  $\equiv\text{FeN}_6=\text{O}$  mediated oxidation process could achieve 97.2% PMS utilization and less affected by the environment factors such as pH and inorganic anions which can lower the operation cost in practical application and reduce the formation of by-products. Meanwhile,  $\equiv\text{Fe}-\text{N}_6/\equiv\text{FeN}_6=\text{O}$  mediated oxidation process is recyclable and stable. Fe-SA/PHCNS achieved long-term degradation of pollutants with negligible ion leaching in continuous flow test which indicates potential practicability of Fe-SA/PHCNS in large-scale water treatment. In a word, Fe-SA/PHCNS has a wide prospect in heterogenous AOPs in terms of cost effectiveness, fast degradation efficiency, sustainability, anti-disturbance capacity and safety.

#### CRediT authorship contribution statement

**Zhi-Wei Wang:** Methodology, Data curation, Formal analysis, Writing – original draft. **Wen-Long Wang:** Validation; Writing – review & editing. **Jin Wang:** Resources, Writing – review & editing. **Yuan Yi:** Software, Investigation. **Qian-Yuan Wu:** Conceptualization, Funding acquisition, Writing - review & editing. **Hong-Ying Hu:** Conceptualization, Funding acquisition, Writing - review & editing.

#### Declaration of Competing Interest

The authors declare that they have no known competing financial interests or personal relationships that could have appeared to influence the work reported in this paper.

#### Acknowledgments

This study was supported by National Natural Science Foundation of

China (No. 52022049/51978370), the Shenzhen Science, Technology and Innovation Commission (No. JCYJ20200109142829123). Thanks to TianHe-2, LvLiang Cloud Computing Center of China for providing computational resource.

#### Appendix A. Supporting information

Supplementary data associated with this article can be found in the online version at doi:10.1016/j.apcatb.2021.121049.

#### References

- [1] C. Liu, D. Kong, P.-C. Hsu, H. Yuan, H.-W. Lee, Y. Liu, H. Wang, S. Wang, K. Yan, D. Lin, Rapid water disinfection using vertically aligned  $\text{MoS}_2$  nanofilms and visible light, *Nat. Nanotechnol.* 11 (2016) 1098–1104.
- [2] Y. Feng, D. Wu, Y. Deng, T. Zhang, K. Shih, Sulfate radical-mediated degradation of sulfadiazine by  $\text{CuFeO}_2$  rhombohedral crystal-catalyzed peroxymonosulfate: synergistic effects and mechanisms, *Environ. Sci. Technol.* 50 (2016) 3119–3127.
- [3] B. Qiao, A. Wang, X. Yang, L.F. Allard, Z. Jiang, Y. Cui, J. Liu, J. Li, T. Zhang, Single-atom catalysis of CO oxidation using  $\text{Pt}_1/\text{FeO}_x$ , *Nat. Chem.* 3 (2011) 634–641.
- [4] S. Mitchell, E. Vorobyeva, J. Pérez-Ramírez, The multifaceted reactivity of single-atom heterogeneous catalysts, *Angew. Chem.* 57 (2018) 15316–15329.
- [5] S.M. Rogge, A. Bayvkina, J. Hájek, H. García, A.I. Olivos-Suárez, A. Sepúlveda-Escribano, A. Vimont, G. Clet, P. Bazin, F. Kapteijn, Metal–organic and covalent organic frameworks as single-site catalysts, *Chem. Soc. Rev.* 46 (2017) 3134–3184.
- [6] H. Yamashita, K. Mori, Y. Kuwahara, T. Kamegawa, M. Wen, P. Verma, M. Che, Single-site and nano-confined photocatalysts designed in porous materials for environmental uses and solar fuels, *Chem. Soc. Rev.* 47 (2018) 8072–8096.
- [7] Y. Chen, S. Ji, C. Chen, Q. Peng, D. Wang, Y. Li, Single-atom catalysts: synthetic strategies and electrochemical applications, *Joule* 2 (2018) 1242–1264.
- [8] T. Risse, S. Shaikhutdinov, N. Nilius, M. Sterrer, H.-J. Freund, Gold supported on thin oxide films: from single atoms to nanoparticles, *Acc. Chem. Res.* 41 (2008) 949–956.
- [9] A. Wang, J. Li, T. Zhang, Heterogeneous single-atom catalysis, *Nat. Rev. Chem.* 2 (2018) 65–81.
- [10] C. Dong, Y. Li, D. Cheng, M. Zhang, J. Liu, Y.-G. Wang, D. Xiao, D. Ma, Supported Metal Clusters: Fabrication and Application in Heterogeneous Catalysis, *ACS Catal.* 10 (2020) 11011–11045.
- [11] G. Mamba, A. Mishra, Graphitic carbon nitride ( $\text{g-C}_3\text{N}_4$ ) nanocomposites: a new and exciting generation of visible light driven photocatalysts for environmental pollution remediation, *Appl. Catal. B.* 198 (2016) 347–377.
- [12] D. Masih, Y. Ma, S. Rohani, Graphitic  $\text{C}_3\text{N}_4$  based noble-metal-free photocatalyst systems: a review, *Appl. Catal. B.* 206 (2017) 556–588.
- [13] Z.-M. Wang, H. Ooga, T. Hirotsu, W.-L. Wang, Q.Y. Wu, H.-Y. Hu, Matrix-enhanced adsorption removal of trace BPA by controlling the interlayer hydrophobic environment of montmorillonite, *Appl. Clay Sci.* 104 (2015) 81–87.
- [14] Y. Zheng, L. Lin, B. Wang, X. Wang, Graphitic carbon nitride polymers toward sustainable photoredox catalysis, *Angew. Chem.* 54 (2015) 12868–12884.
- [15] T. Zhang, D. Zhang, X. Han, T. Dong, X. Guo, C. Song, R. Si, W. Liu, Y. Liu, Z. Zhao, Preassembly strategy to fabricate porous hollow carbonitride spheres inlaid with single  $\text{Cu}-\text{N}_3$  sites for selective oxidation of benzene to phenol, *J. Am. Chem. Soc.* 140 (2018) 16936–16940.
- [16] X. Li, X. Huang, S. Xi, S. Miao, J. Ding, W. Cai, S. Liu, X. Yang, H. Yang, J. Gao, Single cobalt atoms anchored on porous N-doped graphene with dual reaction sites for efficient Fenton-like catalysis, *J. Am. Chem. Soc.* 140 (2018) 12469–12475.
- [17] S. An, G. Zhang, T. Wang, W. Zhang, K. Li, C. Song, J.T. Miller, S. Miao, J. Wang, X. Guo, High-density ultra-small clusters and single-atom Fe sites embedded in graphitic carbon nitride ( $\text{g-C}_3\text{N}_4$ ) for highly efficient catalytic advanced oxidation processes, *ACS nano* 12 (2018) 9441–9450.
- [18] J. Wang, Z. Bai, Fe-based catalysts for heterogeneous catalytic ozonation of emerging contaminants in water and wastewater, *Chem. Eng. J.* 312 (2017) 79–98.
- [19] J. Wang, J. Tang, Fe-based Fenton-like catalysts for water treatment: preparation, characterization and modification, *Chemosphere* (2021), 130177.
- [20] L.S. Zhang, X.H. Jiang, Z.A. Zhong, L. Tian, Q. Sun, Y.T. Cui, X. Lu, J.P. Zou, S. L. Luo, Carbon nitride supported high-loading Fe single-atom catalyst for activation of peroxymonosulfate to generate  $\text{1O}_2$  with 100% selectivity, *Angew. Chem.* 60 (2021) 21751–21755.
- [21] G. Lei, W. Zhao, L. Shen, S. Liang, C. Au, L. Jiang, Isolated iron sites embedded in graphitic carbon nitride ( $\text{g-C}_3\text{N}_4$ ) for efficient oxidative desulfurization, *Appl. Catal. B.* 267 (2020), 118663.
- [22] H. Li, C. Shan, B. Pan, Fe (III)-doped  $\text{g-C}_3\text{N}_4$  mediated peroxymonosulfate activation for selective degradation of phenolic compounds via high-valent iron-oxo species, *Environ. Sci. Technol.* 52 (2018) 2197–2205.
- [23] N. Jiang, H. Xu, L. Wang, J. Jiang, T. Zhang, Nonradical Oxidation of Pollutants with Single-Atom-Fe (III)-Activated Persulfate: Fe (V) Being the Possible Intermediate Oxidant, *Environ. Sci. Technol.* 54 (2020) 14057–14065.
- [24] S. Liang, L. Zhu, J. Hua, W. Duan, P.-T. Yang, S.-L. Wang, C. Wei, C. Liu, C. Feng,  $\text{Fe}^{2+}/\text{HClO}$  reaction produces  $\text{Fe}^{\text{IV}}\text{O}_2^{4-}$ : an enhanced advanced oxidation process, *Environ. Sci. Technol.* 54 (2020) 6406–6414.
- [25] K. Qian, H. Chen, W. Li, Z. Ao, Y.-n Wu, X. Guan, Single-atom Fe catalyst outperforms its homogeneous counterpart for activating peroxymonosulfate to

- achieve effective degradation of organic contaminants, *Environ. Sci. Technol.* 55 (2021) 7034–7043.
- [26] X. Peng, J. Wu, Z. Zhao, X. Wang, H. Dai, L. Xu, G. Xu, Y. Jian, F. Hu, Activation of peroxymonosulfate by single-atom Fe-g-C<sub>3</sub>N<sub>4</sub> catalysts for high efficiency degradation of tetracycline via nonradical pathways: Role of high-valent iron-oxo species and Fe-N<sub>x</sub> sites, *Chem. Eng. J.* 427 (2022), 130803.
- [27] O. Pestovsky, A. Bakac, Reactivity of aqueous Fe (IV) in hydride and hydrogen atom transfer reactions, *J. Am. Chem. Soc.* 126 (2004) 13757–13764.
- [28] Y.D. Perfiliev, E.M. Benko, D.A. Pankratov, V.K. Sharma, S.K. Dedushenko, Formation of iron (VI) in ozonalysis of iron (III) in alkaline solution, *Inorg. Chim. Acta* 360 (2007) 2789–2791.
- [29] C. Adamo, V. Barone, Toward reliable density functional methods without adjustable parameters: The PBE0 model, *J. Chem. Phys.* 110 (1999) 6158–6170.
- [30] L. Goerigk, S. Grimme, Efficient and accurate double-hybrid-meta-gga density functionals · evaluation with the extended GMTKN30 database for general main group thermochemistry, kinetics, and noncovalent interactions, *J. Chem. Theory Comput.* 7 (2011) 291–309.
- [31] M.J. Frisch, G.W. Trucks, H.B. Schlegel, G.E. Scuseria, M.A. Robb, J.R. Cheeseman, G. Scalmani, V. Barone, G.A. Petersson, H. Nakatsuji, X. Li, M. Caricato, A.V. Marenich, J. Bloino, B.G. Janesko, R. Gomperts, B. Mennucci, H.P. Hratchian, J.V. Ortiz, A.F. Izmaylov, J.L. Sonnenberg, Williams, F. Ding, F. Lipparini, F. Egidi, J. Goings, B. Peng, A. Petrone, T. Henderson, D. Ranasinghe, V.G. Zakrzewski, J. Gao, N. Rega, G. Zheng, W. Liang, M. Hada, M. Ehara, K. Toyota, R. Fukuda, J. Hasegawa, M. Ishida, T. Nakajima, Y. Honda, O. Kitao, H. Nakai, T. Vreven, K. Throssell, J.A. Montgomery Jr., J.E. Peralta, F. Ogliaro, M.J. Bearpark, J.H. Heyd, E.N. Brothers, K.N. Kudin, V.N. Staroverov, T.A. Keith, R. Kobayashi, J. Normand, K. Raghavachari, A.P. Rendell, J.C. Burant, S.S. Iyengar, J. Tomasi, M. Cossi, J.M. Millam, M. Klene, C. Adamo, R. Cammi, J.W. Ochterski, R.L. Martin, K. Morokuma, O. Farkas, J.B. Foresman, D.J. Fox, Gaussian 16 Rev. C.01, Wallingford, CT, 2016.
- [32] T. Lu, F. Chen, Multiwin: a multifunctional wavefunction analyzer, *J. Comput. Chem.* 33 (2012) 580–592.
- [33] C.I. Bayly, P. Cieplak, W. Cornell, P.A. Kollman, A well-behaved electrostatic potential based method using charge restraints for deriving atomic charges: the RESP model, *J. Phys. Chem.* 97 (1993) 10269–10280.
- [34] R.F.W. Bader, R.F. Bader, Atoms in Molecules: A Quantum Theory, Clarendon Press, 1990.
- [35] W. Humphrey, A. Dalke, K. Schulten, VMD: visual molecular dynamics, *J. Mol. Evol.* 14 (1996) 33–38.
- [36] A.J. Thom, E.J. Sundstrom, M. Head-Gordon, LOBA: a localized orbital bonding analysis to calculate oxidation states, with application to a model water oxidation catalyst, *Phys. Chem. Chem. Phys.* 11 (2009) 11297–11304.
- [37] K.B. Wiberg, Application of the pople-santyr-segal CNDO method to the cyclopropylcarbinyl and cyclobutyl cation and to bicyclobutane, *Tetrahedron* 24 (1968) 1083–1096.
- [38] J. Xu, Q. Zeng, Two-dimensional (2D) supramolecular coordination at liquid/solid interfaces studied by scanning tunneling microscopy, *Chin. J. Chem.* 33 (2015) 53–58.
- [39] F. Li, G.-F. Han, H.-J. Noh, S.-J. Kim, Y. Lu, H.Y. Jeong, Z. Fu, J.-B. Baek, Boosting oxygen reduction catalysis with abundant copper single atom active sites, *Energy Environ. Sci.* 11 (2018) 2263–2269.
- [40] P. Yin, T. Yao, Y. Wu, L. Zheng, Y. Lin, W. Liu, H. Ju, J. Zhu, X. Hong, Z. Deng, Single cobalt atoms with precise N-coordination as superior oxygen reduction reaction catalysts, *Angew. Chem.* 128 (2016) 10958–10963.
- [41] Y. Chen, S. Ji, Y. Wang, J. Dong, W. Chen, Z. Li, R. Shen, L. Zheng, Z. Zhuang, D. Wang, Isolated single iron atoms anchored on N-doped porous carbon as an efficient electrocatalyst for the oxygen reduction reaction, *Angew. Chem.* 56 (2017) 6937–6941.
- [42] Y.S. Jun, E.Z. Lee, X. Wang, W.H. Hong, G.D. Stucky, A. Thomas, From melamine-cyanuric acid supramolecular aggregates to carbon nitride hollow spheres, *Adv. Funct. Mater.* 23 (2013) 3661–3667.
- [43] Y. Guo, J. Li, Y. Yuan, L. Li, M. Zhang, C. Zhou, Z. Lin, A rapid microwave-assisted thermolysis route to highly crystalline carbon nitrides for efficient hydrogen generation, *Angew. Chem.* 128 (2016) 14913–14917.
- [44] S. Hu, X. Chen, Q. Li, F. Li, Z. Fan, H. Wang, Y. Wang, B. Zheng, G. Wu, Fe<sup>3+</sup> doping promoted N<sub>2</sub> photofixation ability of honeycombed graphitic carbon nitride: the experimental and density functional theory simulation analysis, *Appl. Catal. B.* 201 (2017) 58–69.
- [45] X. Wang, K. Maeda, A. Thomas, K. Takanabe, G. Xin, J.M. Carlsson, K. Domen, M. Antonietti, A metal-free polymeric photocatalyst for hydrogen production from water under visible light, *Nat. Mater.* 8 (2009) 76–80.
- [46] M. Shalom, S. Inal, C. Fettkenhauer, D. Neher, M. Antonietti, Improving carbon nitride photocatalysis by supramolecular preorganization of monomers, *J. Am. Chem. Soc.* 135 (2013) 7118–7121.
- [47] P. Niu, G. Liu, H.-M. Cheng, Nitrogen vacancy-promoted photocatalytic activity of graphitic carbon nitride, *J. Phys. Chem. C.* 116 (2012) 11013–11018.
- [48] W.-J. Ong, L.-L. Tan, Y.-H. Ng, S.-T. Yong, S.-P. Chai, Graphitic carbon nitride (g-C<sub>3</sub>N<sub>4</sub>)-based photocatalysts for artificial photosynthesis and environmental remediation: are we a step closer to achieving sustainability? *Chem. Rev.* 116 (2016) 7159–7329.
- [49] W.-J. Jiang, L. Gu, L. Li, Y. Zhang, X. Zhang, L.-J. Zhang, J.-Q. Wang, J.-S. Hu, Z. Wei, L.-J. Wan, Understanding the high activity of Fe-N-C electrocatalysts in oxygen reduction: Fe/Fe<sub>2</sub>C nanoparticles boost the activity of Fe-N<sub>x</sub>, *J. Am. Chem. Soc.* 138 (2016) 3570–3578.
- [50] J. Li, S. Ghoshal, W. Liang, M.-T. Sougrati, F. Jaouen, B. Halevi, S. McKinney, G. McCool, C. Ma, X. Yuan, Structural and mechanistic basis for the high activity of Fe-N-C catalysts toward oxygen reduction, *Energy Environ. Sci.* 9 (2016) 2418–2432.
- [51] K. Artyushkova, A. Serov, S. Rojas-Carbonell, P. Atanassov, Chemistry of multitudinous active sites for oxygen reduction reaction in transition metal–nitrogen–carbon electrocatalysts, *J. Phys. Chem. C.* 119 (2015) 25917–25928.
- [52] X. Wang, X. Chen, A. Thomas, X. Fu, M. Antonietti, Metal-containing carbon nitride compounds: a new functional organic–metal hybrid material, *Adv. Mater.* 21 (2009) 1609–1612.
- [53] D. Dai, Z. Yang, Y. Yao, L. Chen, G. Jia, L. Luo, Highly efficient removal of organic contaminants based on peroxymonosulfate activation by iron phthalocyanine: mechanism and the bicarbonate ion enhancement effect, *Catal. Sci. Technol.* 7 (2017) 934–942.
- [54] J. Wang, S. Wang, Reactive species in advanced oxidation processes: Formation, identification and reaction A, *Chem. Eng. J.* (2020), 126158.
- [55] Y. Gao, Y. Zhu, L. Lyu, Q. Zeng, X. Xing, C. Hu, Electronic structure modulation of graphitic carbon nitride by oxygen doping for enhanced catalytic degradation of organic pollutants through peroxymonosulfate activation, *Environ. Sci. Technol.* 52 (2018) 14371–14380.
- [56] Y. Pan, Z. Dong, Y. Pan, Y. Zhang, Nitrilotriacetic acid enhanced UV/Fe<sub>0</sub>/H<sub>2</sub>O<sub>2</sub> process for salty wastewater treatment at neutral pH, *Water Cycle* (2021).
- [57] Y. Li, Y. Pan, L. Lian, S. Yan, W. Song, X. Yang, Photosensitized degradation of acetaminophen in natural organic matter solutions: the role of triplet states and oxygen, *Water Res.* 109 (2017) 266–273.
- [58] W. Yang, S.B. Abdelmelek, Z. Zheng, T. An, D. Zhang, W. Song, Photochemical transformation of terbutaline (pharmaceutical) in simulated natural waters: degradation kinetics and mechanisms, *Water Res.* 47 (2013) 6558–6565.
- [59] H.-H. Kim, H. Lee, D. Lee, Y.-J. Ko, H. Woo, J. Lee, C. Lee, A.L.-T. Pham, Activation of hydrogen peroxide by a titanium oxide-supported iron catalyst: evidence for surface Fe (IV) and its selectivity, *Environ. Sci. Technol.* 54 (2020) 15424–15432.
- [60] F. Bonnot, E. Tremey, D. Von Stetten, S. Rat, S. Duval, P. Carpentier, M. Clemancey, A. Desbois, V. Nivière, Formation of high-valent iron-oxo species in superoxide reductase: characterization by resonance raman spectroscopy, *Angew. Chem.* 53 (2014) 5926–5930.
- [61] K. Nakamoto, Resonance Raman spectra and biological significance of high-valent iron (IV, V) porphyrins, *Coord. Chem. Rev.* 226 (2002) 153–165.
- [62] C. Piquer, M. Laguna-Marco, A.G. Roca, R. Boada, C. Guglieri, J. Chaboy, Fe K-edge X-ray absorption spectroscopy study of nanosized nominal magnetite, *J. Phys. Chem. C.* 118 (2014) 1332–1346.
- [63] D. Pearson, C. Ahn, B. Fultz, White lines and d-electron occupancies for the 3d and 4d transition metals, *Phys. Rev. B* 47 (1993) 8471.
- [64] S.-Y. Pang, J. Jiang, J. Ma, Oxidation of sulfoxides and arsenic (III) in corrosion of nanoscale zero valent iron by oxygen: evidence against ferryl ions (Fe (IV)) as active intermediates in Fenton reaction, *Environ. Sci. Technol.* 45 (2011) 307–312.
- [65] H. Huang, D. Sommerfeld, B.C. Dunn, E.M. Eyring, C.R. Lloyd, Ferrate (VI) oxidation of aqueous phenol: kinetics and mechanism, *J. Phys. Chem. A.* 105 (2001) 3536–3541.
- [66] J. Chen, Y. Qi, X. Pan, N. Wu, J. Zuo, C. Li, R. Qu, Z. Wang, Z. Chen, Mechanistic insights into the reactivity of Ferrate (VI) with phenolic compounds and the formation of coupling products, *Water Res.* 158 (2019) 338–349.
- [67] M. Ghosh, K. Manoli, J.B. Renaud, L. Sabourin, G. Nakhla, V.K. Sharma, A.K. Ray, Rapid removal of acesulfame potassium by acid-activated ferrate (VI) under mild alkaline conditions, *Chemosphere* 230 (2019) 416–423.
- [68] Y. Zong, Y. Shao, Y. Zeng, B. Shao, L. Xu, Z. Zhao, W. Liu, D. Wu, Enhanced oxidation of organic contaminants by iron (II)-activated periodate: the significance of high-valent iron-oxo species, *Environ. Sci. Technol.* 55 (2021) 7634–7642.
- [69] H. Dong, Y. Li, S. Wang, W. Liu, G. Zhou, Y. Xie, X. Guan, Both Fe (IV) and radicals are active oxidants in the Fe (II)/peroxydisulfate process, *Environ. Sci. Tech. Let.* 7 (2020) 219–224.
- [70] J. Bernadou, B. Meunier, ‘Oxo-hydroxo tautomerism’ as useful mechanistic tool in oxygenation reactions catalysed by water-soluble metalloporphyrins, *Chem. Commun.* (1998) 2167–2173.
- [71] J.T. Groves, High-valent iron in chemical and biological oxidations, *J. Inorg. Biochem.* 100 (2006) 434–447.
- [72] R. Elkacmi, M. Bennajah, Advanced oxidation technologies for the treatment and detoxification of olive mill wastewater: a general review, *J. Water Reuse Desalin.* 9 (2019) 463–505.
- [73] V.K. Sharma, Ferrate (VI) and ferrate (V) oxidation of organic compounds: kinetics and mechanism, *Coord. Chem. Rev.* 257 (2013) 495–510.
- [74] V.K. Sharma, Oxidation of inorganic compounds by ferrate (VI) and ferrate (V): one-electron and two-electron transfer steps, *Environ. Sci. Technol.* 44 (2010) 5148–5152.
- [75] X. Gao, Q. Guo, G. Tang, W. Peng, Y. Luo, D. He, Effects of inorganic ions on the photocatalytic degradation of carbamazepine, *J. Water Reuse Desalin.* 9 (2019) 301–309.
- [76] Y. Jiang, J.E. Goodwill, J.E. Tobaison, D.A. Reckhow, Bromide oxidation by ferrate (VI): The formation of active bromine and bromate, *Water Res.* 96 (2016) 188–197.
- [77] X. Huang, Y. Deng, S. Liu, Y. Song, N. Li, J. Zhou, Formation of bromate during ferrate (VI) oxidation of bromide in water, *Chemosphere* 155 (2016) 528–533.
- [78] D.O. Martíre, P. Caregnato, J. Furlong, P. Allegretti, M.C. Gonzalez, Kinetic study of the reactions of oxoiron (IV) with aromatic substrates in aqueous solutions, *Int. J. Chem. Kinet.* 34 (2002) 488–494.

- [79] F. Jacobsen, J. Holcman, K. Sehested, Reactions of the ferryl ion with some compounds found in cloud water, *Int. J. Chem. Kinet.* 30 (1998) 215–221.
- [80] T.X.H. Le, M. Bechelany, M. Cretin, Carbon felt based-electrodes for energy and environmental applications: a review, *Carbon* 122 (2017) 564–591.
- [81] J. Xu, X. Zheng, Z. Feng, Z. Lu, Z. Zhang, W. Huang, Y. Li, D. Vuckovic, Y. Li, S. Dai, Organic wastewater treatment by a single-atom catalyst and electrolytically produced H<sub>2</sub>O<sub>2</sub>, *Nat. Sustain.* (2020) 1–9.